Phase separation of full-Heusler nanostructures in half-Heusler thermoelectrics and vibrational properties from first-principles calculations

Alexander Page,[1] Ctirad Uher,[1,*] Pierre Ferdinand Poudeu,[2] and Anton Van der Ven[3,†]
[1]*Department of Physics, University of Michigan, Ann Arbor, Michigan 48109, USA*
[2]*Department of Materials Science, University of Michigan, Ann Arbor, Michigan 48109, USA*
[3]*Materials Department, University of California Santa Barbara, Santa Barbara, California, 93106, USA*
(Received 25 June 2015; revised manuscript received 14 September 2015; published 6 November 2015)

Previous studies have indicated that the figure of merit (ZT) of half-Heusler (HH) alloys with composition MNiSn (M = Ti, Zr, or Hf) is greatly enhanced when the alloys contain a nano-scale full-Heusler (FH) MNi_2Sn second phase. However, the formation mechanism of the FHnanostructures in the HH matrix and their vibrational properties are still not well understood. We report on first-principles studies of thermodynamic phase equilibria in the MNiSn-MNi_2Sn pseudobinary system as well as HH and FH vibrational properties. Thermodynamic phase diagrams as functions of temperature and Ni concentration were developed using density functional theory (DFT) combined with a cluster expansion and Monte Carlo simulations. The phase diagrams show very low excess Ni solubility in HH alloys even at high temperatures, which indicates that any Ni excess will decompose into a two-phase mixture of HH and FH compounds. Vibrational properties of HH and FH alloys are compared. Imaginary vibrational modes in the calculated phonon dispersion diagram of $TiNi_2Sn$ indicate a dynamical instability with respect to cubic [001] transverse acoustic modulations. Displacing atoms along unstable vibrational modes in cubic $TiNi_2Sn$ reveals lower-energy structures with monoclinic symmetry. The energy of the monoclinic structures is found to depend strongly on the lattice parameter. The origin of the instability in cubic $TiNi_2Sn$ and its absence in cubic $ZrNi_2Sn$ and $HfNi_2Sn$ is attributed to the small size of the Ti 3d shells compared to those of Zr and Hf atoms. Lattice constants and heat capacities calculated by DFT agree well with experiment.

DOI: 10.1103/PhysRevB.92.174102 PACS number(s): 64.75.Qr, 63.20.dk, 64.10.+h

I. INTRODUCTION

Half-Heusler (HH) alloys are a particularly promising group of intermetallic materials for thermoelectric high-temperature power generation applications because they are made of inexpensive, light-weight, earth-abundant, and environmentally friendly elements. Furthermore, they have robust mechanical properties and intrinsically high power factors [1–6]. The efficiency of a thermoelectric material is governed by the dimensionless figure of merit $ZT = \alpha^2\sigma T/k$, where α is the Seebeck coefficient, σ is the electrical conductivity, T is the temperature, and k is the thermal conductivity. The thermal conductivity can be written as $k = k_L + k_e$ where k_L and k_e are the lattice and electronic contributions to thermal conductivity, respectively. The thermoelectric HH alloys which are studied most extensively are MNiSn (n-type) and MCoSb (p-type), where M = Ti, Zr, or Hf. These compounds form in a MgAgAs structure type [7] (space group $F\bar{4}3m$). The structure can be thought of as four interpenetrating face-centered cubic (fcc) lattices as shown in Fig. 1. In the case of the n-type MNiSn, the M atom is located at (0,0,0), Ni at (1/4,1/4,1/4), and Sn at (1/2,1/2,1/2). The fourth position (3/4,3/4,3/4) remains vacant. If this fourth position is filled with Ni, the related full-Heusler (FH) structure is formed. The FH phase has the general composition MNi_2Sn with a $MnCu_2Al$ structure type (space group $Fm\bar{3}m$). Despite the similarities in their structures and the small lattice mismatch (2%–3%) between the HH and FH structures, they exhibit drastically different physical properties. The HH alloy is often semiconducting with a small band gap [8] whereas the FH compound is metallic [9].

The main obstacle to achieving a high thermoelectric efficiency in HH alloys is their relatively high thermal conductivity. Up to 90% of the overall thermal conductivity is due to lattice vibrations [10]. It is of critical importance to find new methods that reduce k without adversely affecting the electrical properties of HH alloys. It has been demonstrated that isoelectronic substitution on the M site, i.e., substituting Ti, Zr, and Hf with each other, can reduce k_L effectively [4,5,11]. Nevertheless, $ZT > 2$ has still not been achieved in this class of materials. More recently a new strategy which involves using an overstoichiometric amount of Ni in a bulk HH compound has emerged. The excess Ni creates FH nanostructures that make coherent or semicoherent boundaries with the HH matrix [12–14]. Coherent nanostructures are thought to be less detrimental to the electronic transport and thus are beneficial for thermoelectric (TE) materials [15].

Makongo and co-workers [12] found that adding 2% to 3% excess Ni created semicoherent FH nanostructures which simultaneously increased the Seebeck coefficient and the electrical conductivity while slightly decreasing the lattice thermal conductivity. This resulted in an overall 250% increase of ZT compared to the HH bulk at a temperature of 775 K. The authors attributed this enhancement to an energy filtering effect that occurs at the interfaces of the metallic nanoparticles and the bulk semiconducting matrix.

Much is still unknown about the processes that govern the formation of the nanoparticles and the properties at their interfaces that contribute to the enhanced power factor. Furthermore, to be useful in waste heat recovery

*cuher@umich.edu
†avdv@engineering.ucsb.edu

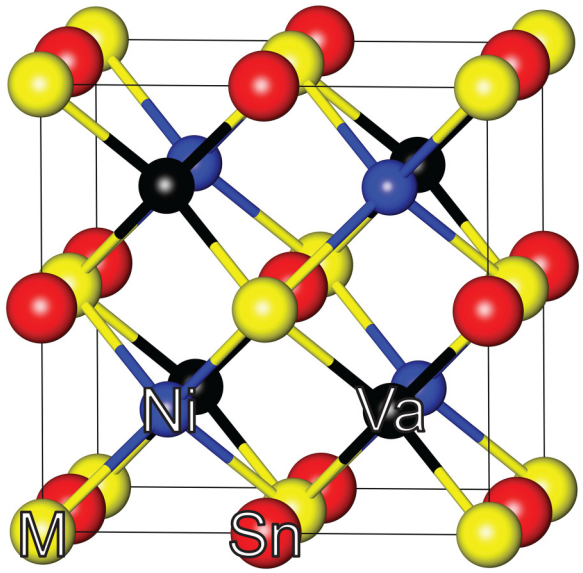

FIG. 1. (Color online) Conventional unit cell of HH compounds with composition MNiSn, where M = Ti, Zr, or Hf. The vacancy site (Va) in the HH phase can be filled with Ni to create the FH structure, MNi_2Sn.

applications, small fractions of FH metallic nanoinclusions must be thermodynamically stable at high temperature within the HH matrix to prevent performance degradation during operation and thermal cycling. In Sec. III A we present results of a study of the equilibrium phase diagram along the pseudobinary composition axis between MNiSn and MNi_2Sn. We combine first-principles electronic structure calculations with statistical mechanics methods to predict phase stability at finite temperature as a function of concentration x in $MNi_{(1+x)}Sn$.

In Sec. III B we investigate vibrational properties of HH and FH structures from first principles. We find that cubic $TiNi_2Sn$ is dynamically unstable while the cubic forms of $ZrNi_2Sn$, and $HfNi_2Sn$ are predicted to be dynamically stable. Structural instabilities have been observed in FH compounds such as $MnNi_2Ga$ before and were explored for their usefulness as potential magnetic shape memory devices [16–18]. The unstable phonon modes we predict in cubic $TiNi_2Sn$ differ qualitatively from those of $MnNi_2Ga$.

II. METHODS

Temperature-composition phase diagrams were calculated for $MNi_{1+x}Sn$ between $x = 0$ (HH) and $x = 1$ (FH) with M = Ti, Zr, and Hf. We used density functional theory (DFT) calculations to parametrize cluster expansion (CE) [19,20] Hamiltonians describing the energy dependence of the crystal on Ni-vacancy disorder over the vacancy sublattice of HH MNiSn. In constructing a cluster expansion, each site on the vacancy sublattice is assigned an occupation variable σ_i that takes a value of 1 or -1 if the site is filled by Ni or is vacant, respectively. The formation energy of any Ni configuration over the vacancy sublattice can then be written exactly as a series expansion in terms of the occupation variables [19] according to

$$E(\vec{\sigma}) = V_0 + \sum_i V_i\sigma_i + \sum_{i,j} V_{i,j}\sigma_i\sigma_j + \sum_{i,j,k} V_{i,j,k}\sigma_i\sigma_j\sigma_k + \cdots = V_0 + \sum_{\{\beta\}} V_\beta\Gamma_\beta(\vec{\sigma}).$$

The polynomials $\Gamma_\beta(\sigma)$ in the above cluster expansion are called cluster basis functions and are defined as the product of occupation variables belonging to a cluster of sites labeled as β. The $\Gamma_\beta(\sigma)$ form a complete and orthonormal basis over the space of all Ni-vacancy configurations on the vacancy sublattice of the HH MNiSn crystal structure [19] The coefficients V_0 and V_β are referred to as effective cluster interactions (ECIs) and are constants to be determined with a first-principles method. Generally, ECIs tend to zero for clusters that connect sites over long distances or for clusters containing a large number of sites. This makes it possible to truncate the cluster expansion after inclusion of 10–20 ECIs corresponding to short-range and compact clusters, such as pairs, triplets, and quadruplets. The ECI of a truncated expansion can then be fitted to fully relaxed DFT energies of different Ni-vacancy configurations. Once fitted, the set of ECIs can be used in Monte Carlo simulations to predict the energy of any configuration of Ni atoms on the vacancy sublattice. Monte Carlo simulations enable the calculation of thermodynamic averages that can be used to calculate the free energies needed to construct temperature-composition phase diagrams.

DFT was also used to parametrize the force constant matrices of harmonic phonon Hamiltonians. Dynamical matrices, constructed with the DFT parametrized force constants, were then diagonalized to determine phonon dispersion curves and phonon densities of states.

The DFT calculations for both the CE and phonon calculations were performed with the Vienna *ab initio* simulation package (VASP) [21] within the generalized gradient approximation (GGA) as parametrized by Perdew, Burke, and Ernzerhof [22] with the projector augmented wave method [23,24]. A plane-wave energy cutoff of 550 eV and a Monkhorst-Pack [25] mesh of $9 \times 9 \times 9$ was used to sample electronic states in the Brillouin zone, which were found to be well converged. Spin-polarized calculations were run on the pure structures (Ti, Zr, and Hf for both HH and FH phases) and all were found to have a net magnetization of zero and negligible energy differences such that all calculations discussed here do not consider spin polarization.

The clusters approach to statistical mechanics (CASM) software package [26] was used to enumerate symmetrically distinct Ni-vacancy configurations over the vacancy sublattice of HH MNiSn, to fit [27] the cluster expansion coefficients to fully relaxed DFT energies, and to perform the Monte Carlo simulations. In this work, we parametrized a cluster expansion for each $MNi_{1+x}Sn$ system with M = Ti, Zr, and Hf. Each expansion was fitted to over 40 DFT calculated structures with supercell volumes up to five times the primitive cell. The optimized set of ECIs was determined by minimizing a

cross-validation (CV) score calculated using the "leave one out" method. The CV scores for each cluster expansion were smaller than 6 meV/site.

Force constant matrices for harmonic vibrational Hamiltonians were fitted to Hellmann-Feynman forces calculated with VASP on supercells in which individual atoms were displaced away from their equilibrium position. The open-source PHONOPY [28] code was used to generate the displaced supercells and fit the force-displacement data to compute the dynamical matrix. A displacement distance of 0.03 Å was used on supercells of dimension $2 \times 2 \times 2$ primitive unit cells ($3 \times 3 \times 3$ for $TiNi_2Sn$). Structural relaxations were performed such that all forces were less than 1×10^{-5} eV/Å before displacing atoms. Born effective charge and dielectric constants for the nonanalytical term correction were calculated using density functional perturbation theory [29,30] in VASP. The constant-volume heat capacity was calculated as a function of temperature using phonon frequencies sampled on a $51 \times 51 \times 51$ Monkhorst-Pack mesh. Structures were visualized using the VESTA software [31].

III. RESULTS AND ANALYSIS

A. Pseudobinary phase stability

Fully relaxed lattice constants for the HH and FH structures are shown in Table I. The calculated DFT parameters overestimate the experimental values [32] by a small margin (0.5%−0.7%) as is to be expected with DFT and the GGA. The DFT formation energies relative to HH MNiSn and FH MNi_2Sn are shown in Fig. 2 as blue diamonds. The CE predicted energies of different Ni-vacancy arrangements over the vacancy sublattice of HH MNiSn are shown as red dots.

The DFT formation energies (relative to HH and FH) of all calculated configurations are positive, confirming that no solid solution or intermediate ordered arrangement of Ni and vacancies is stable between $x = 0$ and 1 at zero temperature. The cluster expansions fitted to the DFT formation energies included 11, 12, and 14 ECIs, resulting in CV scores of 5.7, 4.3, and 5.9 meV for $TiNi_{1+x}Sn$, $ZrNi_{1+x}Sn$, and $HfNi_{1+x}Sn$, respectively.

The DFT formation energies of $ZrNi_{1+x}Sn$ and $HfNi_{1+x}Sn$ exhibit a slight asymmetry around $x = 1/2$. The formation energy associated with adding Ni to the vacancy sublattice in HH ZrNiSn and HfNiSn is higher than that of adding Ni vacancies to FH $ZrNi_2Sn$ and $HfNi_2Sn$, indicating that vacancy defects in the FH are less costly than Ni defects in HH structures [33] The formation energies of the $TiNi_{1+x}Sn$ system, in contrast, are far more symmetrical.

TABLE I. The first two columns show DFT calculated lattice constants from this work compared to experimental values [32]. The second two columns list the lattice mismatch between the HH and FH compounds relative to the HH lattice constant.

	a (Å)		HH-FH mismatch (%)	
	DFT	Expt. [32]	DFT	Expt. [32]
TiNiSn	5.945	5.92	2.97	2.87
ZrNiSn	6.153	6.11	2.61	2.62
HfNiSn	6.113	6.07	2.62	2.80
$TiNi_2Sn$	6.116	6.09		
$ZrNi_2Sn$	6.314	6.27		
$HfNi_2Sn$	6.273	6.24		

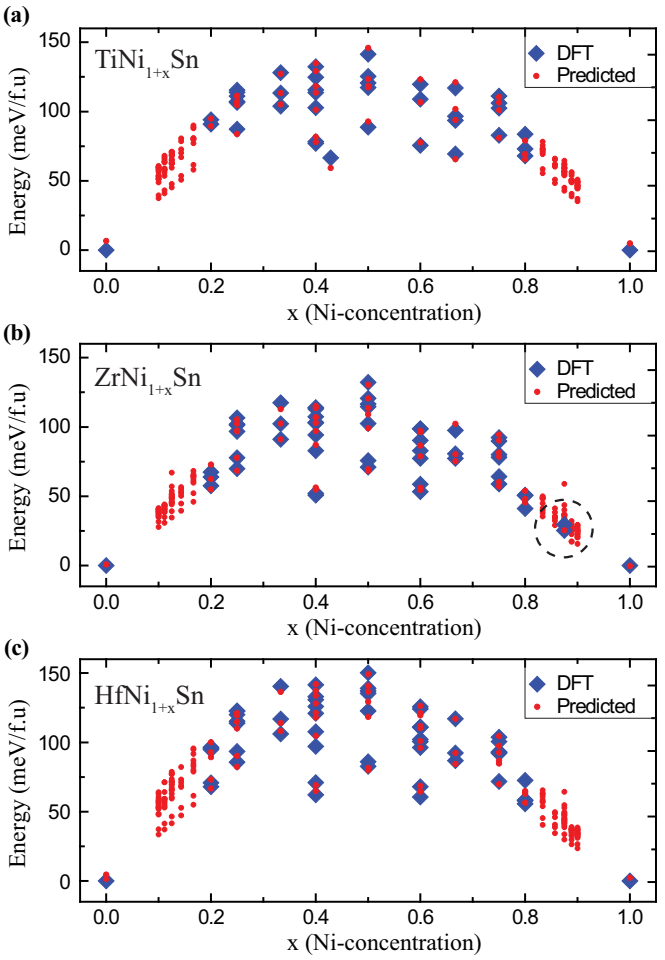

FIG. 2. (Color online) Formation energy per formula unit cell relative to the ground states for $TiNi_{1+x}Sn$ (a), $ZrNi_{1+x}Sn$ (b), and $HfNi_{1+x}Sn$ (c). DFT calculated energies are shown as blue diamonds. The CE predicted energies for the DFT structures and further predictions for configurations up to $x = 0.1$ and $x = 0.9$ are shown as red dots. The dashed circle in (b) indicates specific configurations discussed in the text.

Figure 2 also shows formation energies predicted with the cluster expansion for Ni-vacancy arrangements in larger supercells than those calculated with DFT. Large supercells can accommodate Ni-vacancy configurations at dilute concentrations (i.e., close to $x = 0$ or $x = 1$). The DFT energies of several of the $ZrNi_{1-x}Sn$ configurations were predicted to have low energy by the cluster expansion at $x = 0.875$. Two of the configurations were calculated with VASP to further assess the accuracy of the cluster expansion [data circled by the dashed line in Fig. 2(b)]. The DFT results match the cluster expansion predictions within 4 meV/f.u.

Calculated pseudobinary HH-FH phase diagrams for $TiNi_{1+x}Sn$, $ZrNi_{1+x}Sn$, and $HfNi_{1+x}Sn$ are shown in Fig. 3. The small black diamonds represent calculated phase boundaries while the dashed horizontal lines indicate experimentally

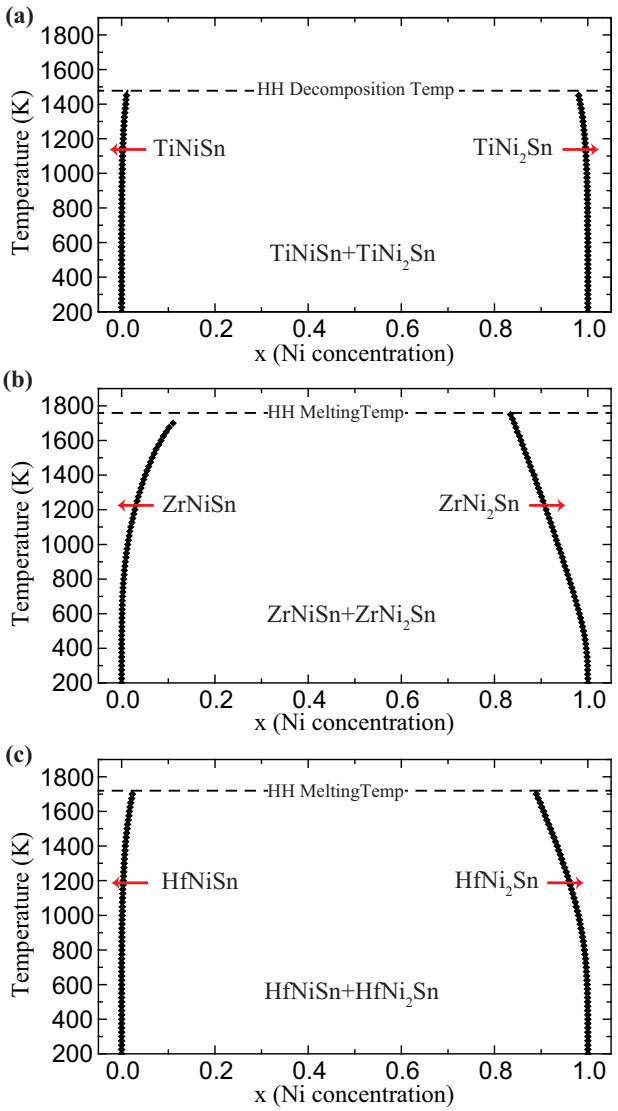

FIG. 3. (Color online) Temperature-concentration pseudobinary phase diagrams of $TiNi_{1+x}Sn$ (a), $ZrNi_{1+x}Sn$ (b), and $HfNi_{1+x}Sn$ (c). The small black diamonds represent calculated points along the phase boundary and the horizontal dashed line indicates experimental melting points for the HH compound.

observed HH melting points [34] (or the decomposition point for TiNiSn). In all three systems, a large miscibility gap separates HH from FH. In the $TiNi_{1+x}Sn$ phase diagram [Fig. 3(a)] a symmetrical and large miscibility gap is predicted over the entire temperature range where TiNiSn is observed to be thermodynamically stable. At 1453 K TiNiSn is experimentally observed to decompose into $TiNi_2Sn$, Ti_2Sn, and Sn [34]. The solubility limit of excess Ni in the HH structure is negligible at 300 K and increases to only 1.0% ($x = 0.010$) at 1450 K. This is in stark contrast to the $ZrNi_{1+x}Sn$ phase diagram where the solubility of Ni is predicted to have a stronger temperature dependence [Fig. 3(b)]. At 300 K, the solubility is also negligible but steadily increases to 5.8% at 1450 K. The solubility continues to increase to 11.0% at 1700 K (the ZrNiSn melting point is 1760 K). For the Hf phase diagram [Fig. 3(c)], the solubility limit once again is negligible at 300 K, increases to 1.0% at 1450 K, and becomes 2.3% at 1700 K. These low values are in agreement with current experiments where FH second phases have been observed with as little as 3% excess Ni with transmission electron microscopy [12].

Our study suggests that a secondary FH phase will precipitate within a HH matrix at excess Ni concentrations greater than $x = 0.01$ for temperatures up to 1450 K in TiNiSn and HfNiSn, and up to 900 K in ZrNiSn. If precipitation occurs at the nanoscale, the FH phase may be difficult to observe experimentally by x-ray diffraction techniques [13] However, the authors of Ref. [13] argue that the measured HH bulk lattice parameter remains constant for all compositions with $x < 3\%$, suggesting two-phase coexistence.

The temperature dependence of the Zr phase has a larger Ni solid solubility at high temperatures; however, many studies of TE HH materials find *ZT* to peak between 600 and 800 K [4,11,12]. The Zr phase shows only 0.4% solubility at 800 K, implying that FH precipitates are predicted to be stable during high-temperature operation in the temperature range of interest.

The solubility of vacancies in the FH phase is seen to be much larger than the solubility of Ni in the HH phase. This is especially true for the $ZrNi_{1+x}Sn$ and $HfNi_{1+x}Sn$ phase diagrams. All three systems begin with negligible vacancy solubility at 300 K. The $ZrNi_{1+x}Sn$ system shows vacancy solubility of 12% ($x = 0.88$) at 1450 K and 16% ($x = 0.84$) at 1700 K. The $HfNi_{1+x}Sn$ system shows vacancy solubility of 7.3% at 1450 K and 11.0% at 1700 K. The $TiNi_{1+x}Sn$ diagram shows an increase to only 2.0% ($x = 0.980$) at 1450 K. The asymmetry between vacancy solubility in the FH phase and Ni solubility in the HH phase arises from the asymmetry in the formation energies shown in Fig. 2.

The equilibrium phase diagrams calculated here using the CE model are not the only consideration in determining the actual microstructure observed in materials. In some cases a material will never realize its thermodynamically stable state because nucleation and diffusion barriers may prevent formation and subsequent growth of the stable phase in a supersaturated matrix. Our current treatment also neglects contributions to the free energy arising from coherency strains during two-phase coexistence. Coherency strains increase the solubility limits of miscibility gaps [35–38]. The lattice mismatch between HH and FH ranges between 2.5% and 3%, which can result in sizable strain energy penalties during coherent two-phase coexistence, depending on the elastic moduli of the coexisting phases. Strain energies are also very sensitive to the morphology and distribution of coherent precipitates within a matrix [39].

B. Vibrational properties

1. *Half-Heusler lattice dynamics*

Phonon dispersion curves along high-symmetry directions for TiNiSn, ZrNiSn, and HfNiSn structures are shown in Fig. 4. For the semiconducting HH materials we used a nonanalytic correction to account for the dipole-dipole interactions, resulting in the splitting of longitudinal optical (LO) and transverse optical (TO) bands at the zone center. Several trends can be identified in the HH phonon spectra

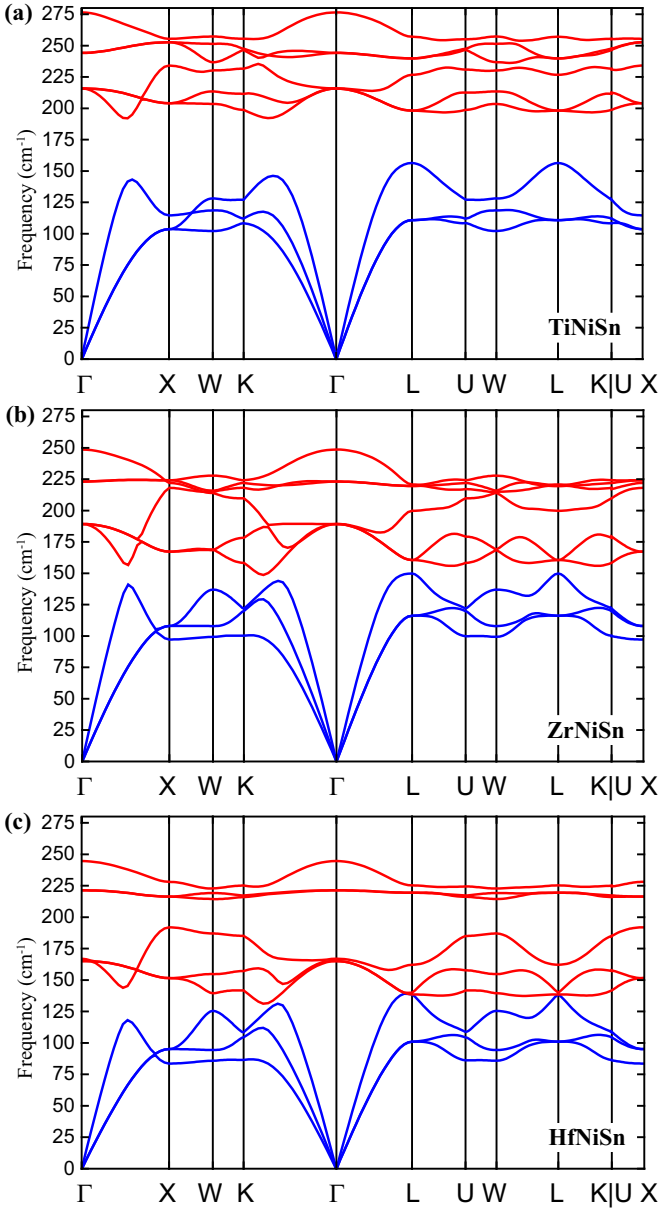

FIG. 4. (Color online) Phonon dispersion curves of TiNiSn (a), ZrNiSn (b), and HfNiSn (c) calculated with DFT shown along high-symmetry paths. Optical bands are shown in red and acoustic in blue.

as the *M* site atom is changed from Ti to Zr to Hf. Most noticeably the wide acoustic-optical band gap which exists in TiNiSn [Fig. 4(a)] near 175 cm^{-1} is closed in ZrNiSn [Fig. 4(b)] as the lower optical modes drop in frequency. Large gaps between the optical and acoustic modes reduce acoustic-optical phonon-phonon scattering [40] and are undesirable for low-thermal-conductivity materials. Gap size generally scales with the mass difference of atoms in the basis. The qualitative similarity in shape of the TiNiSn and ZrNiSn bands shows that the bonding structure is similar and thus the mass difference between Ti and Zr atoms is the primary cause of the frequency shift [41].

In HfNiSn the acoustic and optical bands drop lower in frequency than in ZrNiSn and greater optical-acoustic band mixing is seen. All three acoustic branches of HfNiSn have comparably lower Γ point group velocities than TiNiSn or ZrNiSn as shown in Table II. Also a new gap centered around 200 cm^{-1} is opened between the two sets of optical modes. This suggests that it is possible to tune the location of the lower optical bands by isoelectronic substitution on the *M* site. Phonon-phonon scattering mechanisms become more important at high temperatures and thus are of interest in the search for strategies to lower lattice thermal conductivity in HH alloys. All calculated HH phonon dispersions agree well with past theoretical studies that relied on different computational methods [41,42].

TABLE II. The Debye temperature Θ_D calculated from the phonon density of states compared to experimental results from Ref. [45] (a) and Ref. [44] (b). Group velocities v_g at the zone center were fitted to calculated phonon frequency data along the Γ-*X* direction.

	Θ_D (K)		v_g (cm×10^{5}s^{-1})	
	Calculated	Expt.	LA	TA
TiNiSn	370	335 (a), 407 (b)	5.9	2.8
ZrNiSn	372	323 (b)	5.7	2.9
HfNiSn	320	307 (b)	5.1	1.8
$ZrNi_2Sn$	247		4.7	2.7
$HfNi_2Sn$	266		4.2	2.5

2. *Full-Heusler lattice dynamics*

The calculated dispersion curves for the FH structures, shown in Fig. 5, have three additional optical bands arising from the second Ni atom in the primitive cell, making a total of 12 phonon bands. The dispersion curves for $TiNi_2Sn$ show imaginary frequencies [Fig. 5(a)]. Imaginary phonon frequencies (shown as negative frequencies) indicate dynamical instabilities within the cubic phase at zero kelvin. This surprising result was checked by calculating force constants with larger supercells of size 3 × 3 × 3, which confirmed the existence of the imaginary modes.

Other magnetic and nonmagnetic full-Heusler variants, of interest for magnetic shape memory applications [16–18], have been found to exhibit dynamical instabilities aswell. The $TiNi_2Sn$ phonon dispersions presented here differ from results from a previous computational study by Hermet *et al.* (Ref. [43]). That work uses the local density approximation (LDA), in which no imaginary frequencies were observed. The origins of the instability observed in this work will be further discussed in Sec. IV.

In contrast to $TiNi_2Sn$, the $ZrNi_2Sn$ and $HfNi_2Sn$ phonon spectra have no unstable phonon modes, although both exhibit very low-frequency acoustic modes at the *X* point. The $ZrNi_2Sn$ and $HfNi_2Sn$ dispersion curves show significant mixing between acoustic and optical modes. The lower optical modes appear to push down the acoustic modes, dropping the group velocities below that of HfNiSn as seen in Table II.

3. *Phonon density of states and thermal properties*

The total phonon density of states (DOS) and partial phonon density of states (PDOS) are shown in Fig. 6. The PDOS is

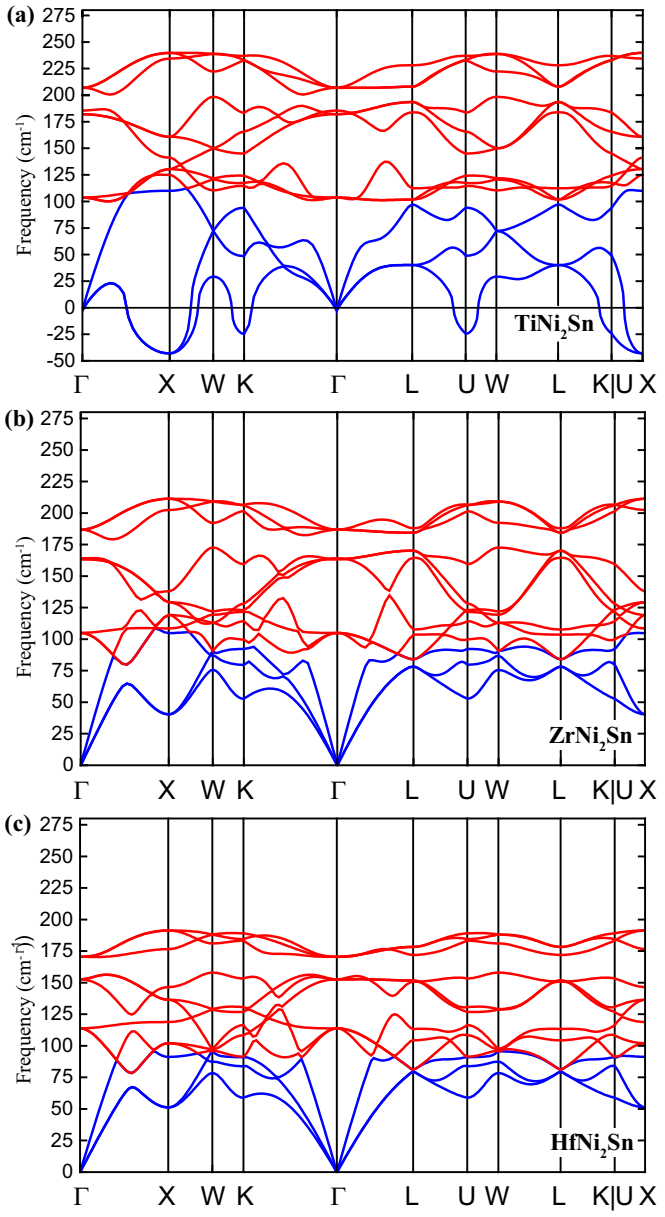

FIG. 5. (Color online) Phonon dispersion curves of $TiNi_2Sn$ (a), $ZrNi_2Sn$ (b), and $HfNi_2Sn$ (c) calculated with DFT shown along high-symmetry paths. Optical bands are shown in red and acoustic in blue. Imaginary frequencies are shown as negative values.

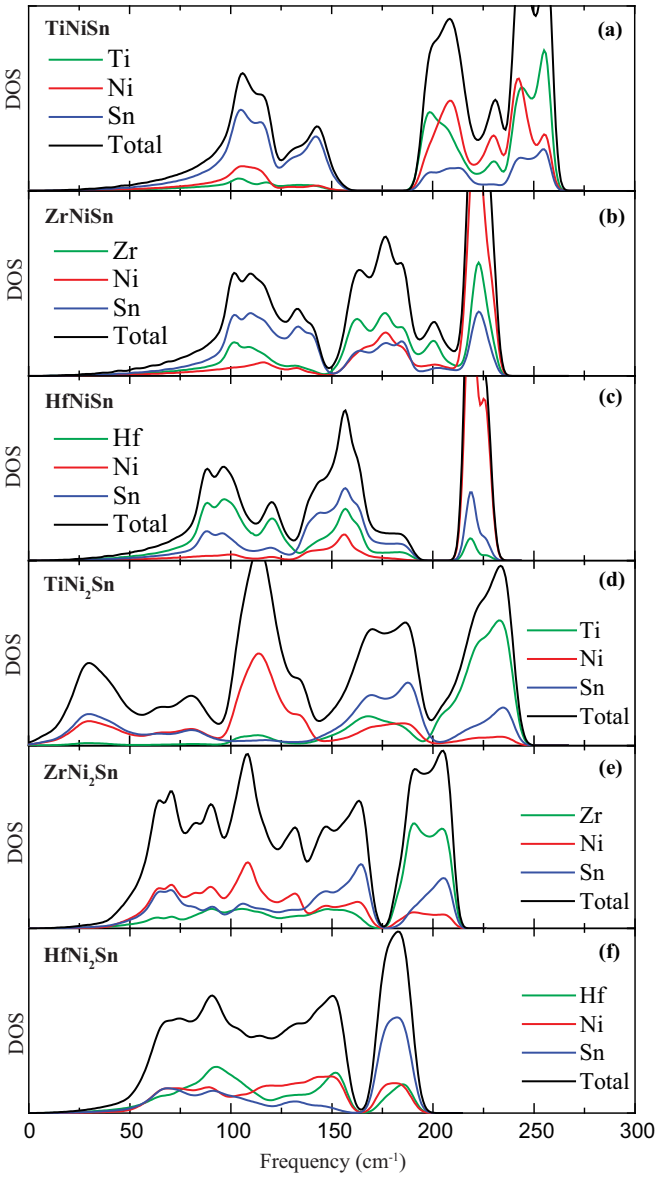

FIG. 6. (Color online) Total density of states (DOS) and partial density of states (PDOS) calculated with DFT. Total DOS is shown in black and contributions from each atom are shown in color, green for M = Ti, Zr, or Hf, red for Ni, and blue for Sn. Parts (a) through (f) show the DOS for TiNiSn, ZrNiSn, HfNiSn, $TiNi_2Sn$, $ZrNi_2Sn$, and $HfNi_2Sn$, respectively.

a measure of the relative contributions of each atom in the eigenvector of motion associated with each phonon mode. The FH structures [Figs. 6(d)–6(f)] are seen to have very mixed states with approximately equal contributions by each atom for the acoustic and first optical bands. The $TiNi_2Sn$ structure has a significant DOS at frequencies below 50 cm^{-1} from the low-frequency TA mode contributions which arise from the instability. The HH compounds [Figs. 6(a)–6(c)] have modes where the PDOS is dominated by contributions from one atom. The trends in the HH DOS reflect those seen in the phonon dispersion curves; the peaks shift to lower frequencies as the mass of the M-site atom increases. The acoustic modes are predominantly formed by the heaviest atom in the basis, which is Sn in TiNiSn and ZrNiSn. However, the mass of Hf atoms is larger than that of Sn and the HfNiSn acoustic modes are dominated by the Hf atom contributions.

The acoustic modes dominate heat transport of materials because of their high group velocities compared to the optical modes. The shift of dominance from Sn to Hf in the acoustic PDOS implies that M-site alloying would have a greater effect on k_L in HfNiSn than in TiNiSn [43]. Previous studies have wide variance in their synthesis techniques and resultant microstructure of their materials, which makes it difficult to confirm the alloying effects on k_L with current experimental results. The optical modes are primarily composed of M and Ni in TiNiSn and ZrNiSn, and switch to Ni and Sn for the HfNiSn structure. The Debye temperature was calculated by

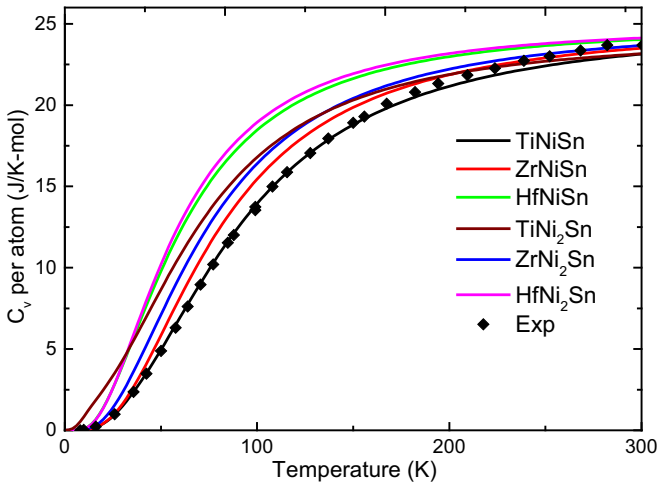

FIG. 7. (Color online) Heat capacity per atom calculated using DFT. TiNiSn results are compared to experimental data [45].

fitting the total DOS from zero to one-quarter of the maximum phonon frequency. The results follow the trend of a decreasing Debye temperature when going from a lighter (Ti) to a heavier (Hf) transition metal. This trend is consistent with a similar increase in phonon DOS at low frequencies with increasing transition metal mass. The calculated Debye temperatures match reasonably well with experimental results [44,45] as shown in Table II.

The phonon contributions to heat capacity at constant volume, C_v, were calculated within the PHONOPY code and are shown in Fig. 7 for temperatures from 0 to 1000 K. The specific heat at constant volume shown in Fig. 12, C_v, is normalized by the number of atoms. The computed C_v of TiNiSn agrees well with experimental measurements [45]. Unfortunately we know of no experimental data available for comparison with the other HH and FH materials. The per atom heat capacities at 100 K are given as $c_v = 13.9$, 15.4, 16.4, 16.7, 18.46, and 18.93 kJ K^{-1} mol^{-1} for TiNiSn, ZrNiSn, HfNiSn, $TiNi_2Sn$, $ZrNi_2Sn$, and $HfNi_2Sn$, respectively. This trend can be explained by the shifting of the vibrational DOS to lower frequencies, which increases the number of modes available at low temperatures. $TiNi_2Sn$ is the exception. The low-frequency modes associated with the X TA instability create a large DOS at frequencies below 50 cm^{-1}, making the c_v of $TiNi_2Sn$ larger than that of the other structures by up to 32 K. Imaginary modes were not included in the calculation of c_v. In the case of HH compounds, increasing the mass of the M-site atom causes the DOS to shift to lower frequencies, and in FH structures the addition of the second Ni atom introduces a new optical band that pushes the acoustic band frequencies lower. As the temperature increases past the Debye temperature, all phonon modes become occupied and the calculated specific heats of all the HH and FH phases approach the classical Dulong-Petit limit of 24.94 within ± 0.04 J mol^{-1}K^{-1} atom^{-1} at 2000 K.

4. $TiNi_2Sn$ instability

(a) Energies of distorted cells. The imaginary phonon frequencies of cubic $TiNi_2Sn$ are a result of the negative curvature of the Born-Oppenheimer energy surface with respect to a particular collective atomic displacement. The cubic $TiNi_2Sn$ crystal structure can therefore further decrease its energy by distorting along the unstable phonon mode. Lower-energy structures obtained in this manner often have a lower symmetry and differ from the high-symmetry structure by a distortion of the unit cell. Many phases that are predicted to be dynamically unstable at zero K with DFT are indeed experimentally observed at high temperatures where they are stabilized by anharmonic vibrational excitations [46–49]. The predicted phonon dispersion curves for $TiNi_2Sn$ show unstable modes near the Brillouin zone edge at the X, K, and U points. At the X point, the phonon wave travels along the cubic [001] direction with a wavelength equal to the conventional cubic unit cell. The unstable modes at the X point correspond to twofold-degenerate transverse acoustic (TA) modes which we denote as X-TA modes. The unstable modes at the K and U points each are singly degenerate longitudinal acoustic (LA) modes.

We can further explore the nature of the dynamical instabilities of cubic $TiNi_2Sn$ by directly calculating the energy of the crystal as a function of the amplitude of the unstable phonon modes. While common Bain paths such as tetragonal and rhombohedral distortions revealed no reduction in the energy of cubic $TiNi_2Sn$, lower-energy structures are found when the atoms are internally shuffled according to the X-point TA mode eigenvectors. The atomic displacements of this phonon mode are shown in Fig. 8, with displacements magnified by 20 times for clarity. The energies of MNi_2Sn (M = Ti, Zr, Hf) as a function of the amplitude of an X-TA phonon mode are shown in Fig. 9(a). Since the X-TA phonon mode is dominated by Ni displacements, we use as a metric of the amplitude of the phonon mode [the horizontal axis in Fig. 9(a)] the displacement of Ni atoms. As is clear in Fig. 9(a), the cubic form of $TiNi_2Sn$

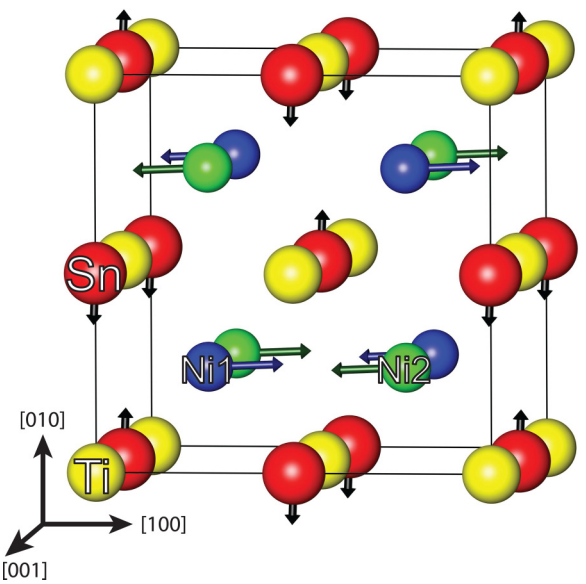

FIG. 8. (Color online) Atomic motions of the X-point TA phonon mode shown for each atom of the $TiNi_2Sn$ structure. The phonon mode travels in the cubic [001] direction, out of the page. Black arrows indicate atomic motion with amplitudes magnified by 20 times.

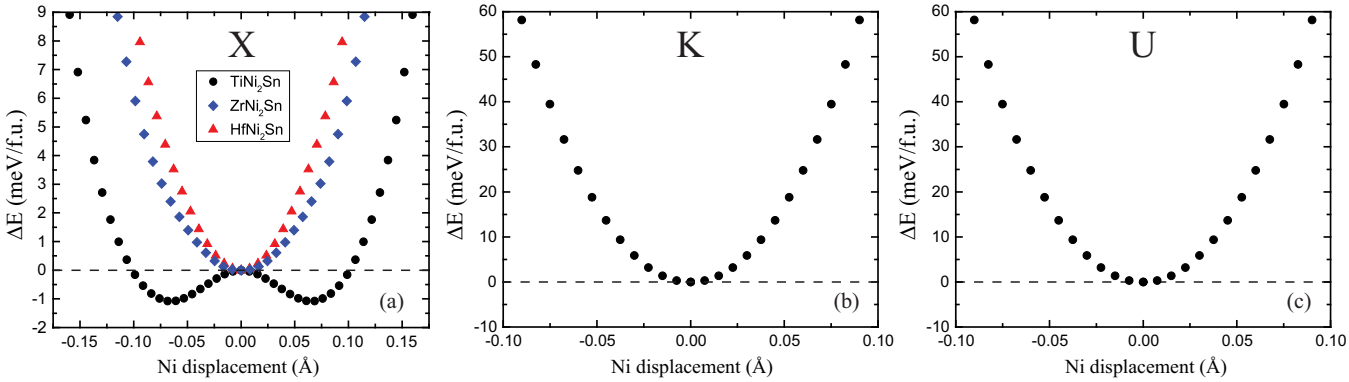

FIG. 9. (Color online) Energy per formula unit of $2 \times 2 \times 2$ supercells is shown as a function of phonon mode displacement amplitude for (a) X-point, (b) K-point, and (c) U-point modes for $TiNi_2Sn$. $ZrNi_2Sn$ and $HfNi_2Sn$ energies are shown in (a) for comparison and have positive curvature along the distortion path, whereas $TiNi_2Sn$ has negative curvature with energies that drop 1.1 meV below that of cubic $TiNi_2Sn$. K and U points show no instabilities along their paths. The horizontal axis measures the displacement of Ni atoms from their equilibrium position.

can further lower its energy by 1.1 meV per formula unit (f.u.). Cubic $ZrNi_2Sn$ and $HfNi_2Sn$ in contrast are dynamically stable for the same X-TA phonon modes [Fig. 9(a)]. Isoelectronic substitution of M-site atoms has little effect on the chemistry of the bonding but does result in significant differences in the atomic radii of atoms. The energy of $TiNi_2Sn$ along the phonon modes having imaginary frequencies at the K and U points increases with amplitude [Figs. 9(b) and 9(c)]. Hence the DFT parametrized harmonic phonon Hamiltonian used to calculate phonon dispersion curves for $TiNi_2Sn$ predicts spurious dynamical instabilities at the K and U points.

The X point is on the Brillouin zone edge in the symmetrically equivalent cubic [001], [010], and [100] directions. Each direction has two orthogonal transverse acoustic modes that we call ε_1 and ε_2. The full energy landscape of the X-TA subspace can be characterized by combinations of these two modes. Figure 10 shows the change in energy (relative to cubic $TiNi_2Sn$) as a function of ε_1 and ε_2 amplitudes. The plot shows that lower-energy distortions exist for any displacements due to a combination of both X-TA ε_1 and ε_2 phonon modes; however, the minimum energies are found along the symmetrically equivalent (ε_1,0) and (0,ε_2) directions. The displacements corresponding to these minima lower the symmetry of cubic $TiNi_2Sn$ to monoclinic. The distorted structure has space group $P2_1/m$ (no. 11). We did not explore whether additional symmetry breaking could reduce the energy of $TiNi_2Sn$ any further.

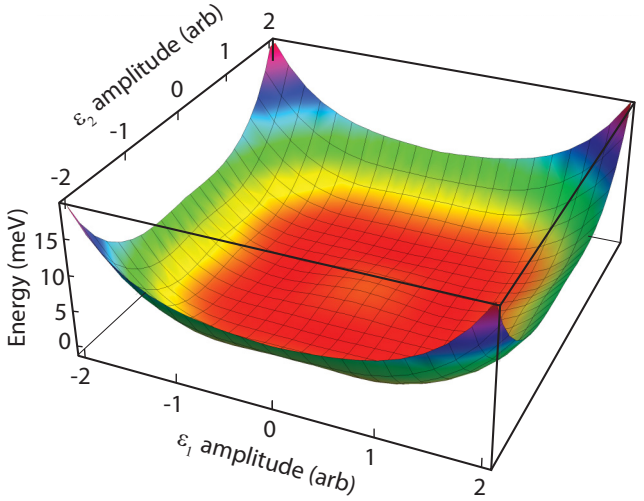

FIG. 10. (Color online) Contour plot shows the change in formation energy of $TiNi_2Sn$ structure as a function of X-TA phonon mode amplitudes ε_1 and ε_2.

The energy landscape in Fig. 9(a) shows not only that $TiNi_2Sn$ is dynamically unstable at zero K, but that anharmonic vibrational excitations at elevated temperature should at some transition temperature result in the stabilization of the high-temperature cubic form of $TiNi_2Sn$. However, the shallow depth of the energy well at only 1.1 meV/f.u. suggests that the critical temperature will be very low if observable at all. A treatment accounting for anharmonic vibrational excitations would be necessary to predict the true critical temperature. While very little is understood about high-temperature phases that become dynamically unstable at low temperature, the anharmonic excitations that are crucial in making these phases stable above a critical temperature should also have a significant impact on their thermal conductivity.

(b) Origins of the instability. To better understand why $ZrNi_2Sn$ and $HfNi_2Sn$ full-Heusler structures are dynamically stable and $TiNi_2Sn$ is not, we explored the effects of interatomic spacing on the $TiNi_2Sn$ instability. As expected, increasing or decreasing the lattice parameter of the cubic FH crystal structure results in an increase in the energy. However, the variation of the energy as a function of X-TA phonon mode amplitude changes dramatically with the lattice parameter. Figure 11 shows the energy of distorted $TiNi_2Sn$ supercells with varying lattice parameter a. It is found that increasing the lattice parameter makes the structure less stable by lowering the energy of the distorted structures relative to the cubic form. Decreasing the lattice parameter to $a = 0.98a_0$ results in all distorted structures having a higher energy than the cubic structure. The transition from negative to positive curvature occurs near $a = 0.99a_0 = 6.054$ Å. The positive energy curvature at these smaller lattice parameters implies that smaller interatomic distances stabilize the cubic structure with respect to the X-TA displacements.

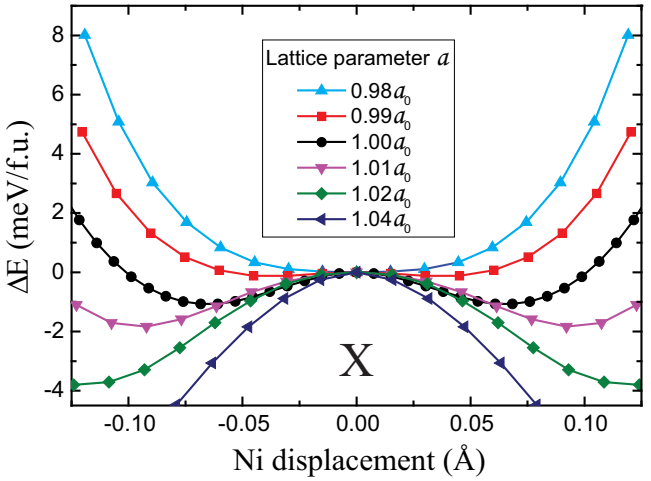

FIG. 11. (Color online) Formation energies of TA-X mode distorted $TiNi_2Sn$ structures relative to the fcc structure shown for cells of varying lattice parameter a, where $a = d * a_0$, $d = 0.98$, 0.99, 1.00, 1.01, 1.02, 1.04, and $a_0 = 6.116$ Å.

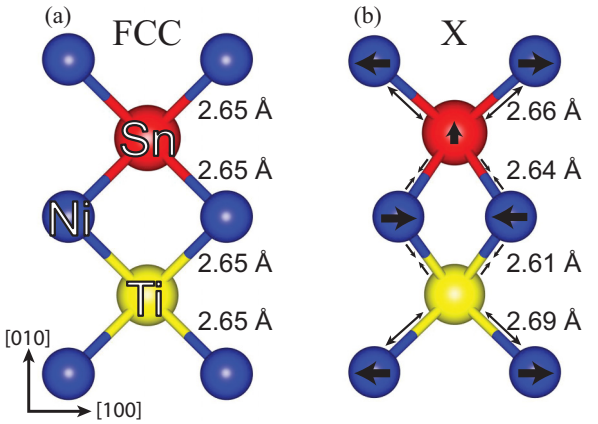

FIG. 12. (Color online) Schematic of the fcc structure (A) and the X-TA mode displaced structure (B), viewed along the cubic [001] direction. The distance between atoms is shown next to each bond. Black arrows centered on atoms show the direction of their displacement relative to the fcc structure.

The results of Ref. [43], which found no complex modes in $TiNi_2Sn$ dispersions, can be explained by the tendency for the X-TA instability to stabilize for smaller lattice parameters. Hermet and co-wokers use LDA functionals, which tend to underestimate lattice parameters. Their LDA lattice parameter of $a = 5.91$ Å, underestimates the experimental value by 3%, which would remove all traces of the instability according to our results. In our work, GGA functionals overestimate the lattice parameter and exceed the experimental value by 0.5%. While the GGA calculations achieve better agreement with experiment in this case, on average the GGA can overestimate the lattice parameter by about 1% [50]. Given the sensitivity of the energy surface tpo the lattice parameter, the results presented here can only claim that the $TiNi_2Sn$ structure is unstable according to GGA calculations.

The instabilities seen in other Heusler alloys were also found to be in TA vibrational modes dominated by the motion of Ni atoms; however the same explanations of optical-acoustic mode mixing cannot be applied to $TiNi_2Sn$ [16,17]. The ordering of the optical bands in MNi_2Sn structures does not change between $TiNi_2Sn$ and $ZrNi_2Sn$ or $HfNi_2Sn$. Furthermore, the Fermi level is not located at a local maximum of the electronic density of states (EDOS) and little to no change in the EDOS is seen near the Fermi level for the distorted structures. Thus the instability cannot be explained by the Jahn-Teller effect either [51]. It is unclear if the Fermi surface nesting proposed for $MnNi_2Ga$ can be applied to $TiNi_2Sn$ [18]. One possible explanation for the instability in $TiNi_2Sn$ is a simple rearrangement of atoms to achieve energetically favorable interatomic distances.

We now examine the effects of X-TA mode distortions on the interatomic distances. In the cubic full-Heusler structure, each Ti (or Sn) site is at the center of a cube made up of eight Ni atoms. The Ti-Ni and Sn-Ni interatomic distances are equal for all eight Ni atoms as shown in Fig. 12(a), where only the top layer of Ni atoms is shown in blue for clarity. To a close approximation the distortion moves Ni atoms only in the [100] directions indicated in Fig. 12(b). Four of the eight Ni atoms slide closer to Ti and shorten the Ti-Ni bond by 0.04 Å. The other four move away and lengthen their bond by 0.04 Å. Sn atoms also move in the X-TA distortion. Sn atoms move away from the oncoming Ni atoms by shifting in the [010] direction. The result is that four Ni-Sn bonds are shortened by only 0.01 Å and the other four lengthened by only 0.01 Å. The overall effects result in Ti atoms being closer to four of the eight Ni atoms while the Ni-Sn bond lengths are more or less unchanged.

Strong p-d hybridization seen in other full-Heusler structures [16,52] may be present in the Ni-Sn bonding and result in more rigid bonds. Rigid Ni-Sn bonds might force the structure to have a higher lattice parameter, leaving the Ti atoms unable to fill the voids. The X-TA distortion path avoids the energy penalty of altering the Ni-Sn bond lengths while moving the Ti atoms into more stable bonds with four of the eight Ni, possibly resulting in the lower formation energies relative to the cubic structure.

IV. CONCLUSIONS

A thorough analysis of equilibrium phases as a function of temperature and Ni concentration was performed using DFT energies combined with a cluster expansion and Monte Carlo simulations on HH-FH systems. The calculated phase diagrams predict a miscibility gap between HH MNiSn and FH MNi_2Sn, with limited Ni solubility in the HH and a limited tolerance for Ni vacancies in the FH. The calculated phase diagrams suggest that the FH nanoprecipitates seen in experiments are thermodynamically stable at concentrations of 1% below the temperature of 1400 K in $TiNi_{1+x}Sn$ and $HfNi_{1+x}Sn$ and below 800 K in $ZrNi_{1+x}Sn$. Higher solubility of vacancies in FH compositions implies that a larger supersaturation is necessary to form a HH second phase inside the FH bulk at elevated temperatures.

Phonon spectra and thermodynamic properties were examined using DFT. The phonon band structures of the HH materials show that the selection of the M atom (M = Ti, Zr, or Hf) changes the frequency of optical bands and determines

which atom dominates the PDOS of acoustic modes. The calculated heat capacity data agree well with experiment for TiNiSn and other MNiSn and MNi_2Sn phases show trends that follow from the shifts in DOS frequency with *M*-site mass.

The $TiNi_2Sn$ structure was predicted to be dynamically unstable at zero K. It is possible to lower the energy compared to cubic FH by displacing atoms along the *X*-TA mode distortion path. The nature of the instability is found to be different from instabilities found in other Heusler compounds. The volume-dependent distortion energies show that smaller lattice parameters remove the instability along the *X*-TA mode, indicating that interatomic distances are crucial in creating the instability. We propose that the instability could originate from the smaller size of the Ti 3*d* orbitals compared to Zr 4*d* and Hf 5*d* orbitals.

ACKNOWLEDGMENTS

The authors would like to acknowledge helpful discussions with Hang Chi, Min-Hua Chen, Alex Emly, and Si Hui, and the ongoing collaboration with co-workers of P. Poudeu and A. Van der Ven. This research is supported by the Department of Energy, Office of Basic Energy Sciences under Award No. DE-SC-0008574.

[1] W. Xie, A. Weidenkaff, X.Tang, Q. Zhang, J. Poon and T. Tritt, Nanomaterials **2**, 379 (2012).
[2] S. Sakurada and N. Shutoh, Appl. Phys. Lett. **86**, 082105 (2005).
[3] H. Hohl, A. Ramirez, W. Kaefer, K. Fess, C. Thurner, C. Kloc, and E. Bucher, in *Thermoelectric Materials—New Directions and Approaches*, edited by T. Tritt *et al.*, MRS Symposia Proceedings No. 478 (Materials Research Society, Pittsburgh, 1997), p. 109.
[4] C. Uher, J. Yang, S. Hu, D. T. Morelli, and G. P. Meisner, Phys. Rev. B **59**, 8615 (1999).
[5] Q. Shen, L. Chen, T. Goto, T. Hirai, J. Yang, G. P. Meisner, and C. Uher, Appl. Phys. Lett. **79**, 4165 (2001).
[6] P. Maji, N. Takas, D. Misra, H. Gabrisch, K. Stokes, and P. Poudeu, J. Solid State Chem. **183**, 1120 (2010).
[7] W. Jeitschko, Metall. Mater. Trans. **1**, 3159 (1970).
[8] S. Ogut and K. M. Rabe, Phys. Rev. B **51**, 10443 (1995).
[9] T. Graf, C. Felser, and S. Parkin, Prog. Solid State Chem. **39**, 1 (2011)
[10] S. Bhattacharya, M. J. Skove, M. Russell, T. M. Tritt, Y. Xia, V. Ponnambalam, S.J. Poon, and N. Thadhani, Phys. Rev. B **77**, 184203 (2008).
[11] M. Schwall and B. Balke, Phys. Chem. Chem. Phys. **15**, 1868 (2013).
[12] J. Makongo, D. Misra, X. Zhou, A Pant, M. Shabetai, X. Su, C. Uher, K. Stokes, and P. Poudeu, J. Am. Chem. Soc. **133**, 18843 (2011).
[13] Y. Liu, P. Sahoo, J. Makongo, X. Zhou, S Kim, H. Chi, C. Uher, X. Pan, and P. Poudeu, J. Am. Chem. Soc. **135**, 7486 (2013).
[14] Y. W. Chai and Y. Kimura, Appl. Phys. Lett. **100**, 033114 (2012).
[15] M. Kanatzidis, Chem. Mater. **22**, 648 (2010).
[16] A. T. Zayak, P. Entel, K. M. Rabe, W. A. Adeagbo, and M Acet, Phys. Rev. B **72**, 054113 (2005).
[17] P. Webster, K. Ziebeck, S. Town, and M. Peak, Philos. Mag. B **49**, 295 (1984).
[18] C. Bungaro, K. M. Rabe, and A. Dal Corso, Phys. Rev. B **68**, 134104 (2003).
[19] J. Sanchez, F. Ducastelle, and D. Gratias, Physica A **128**, 334 (1984).
[20] D. de Fontaine, *Solid State Physics* (Academic, New York, 1994).
[21] G. Kresse and J. Furthmüller, Phys. Rev. B **54**, 11169 (1996).
[22] J. P. Perdew, K. Burke, and M. Ernzerhof, Phys. Rev. Lett. **77**, 3865 (1996).
[23] P. E. Blöchl, Phys. Rev. B **50**, 17953 (1994).
[24] G. Kresse and D. Joubert, Phys. Rev. B **59**, 1758 (1999).
[25] H. Monkhorst and J. Pack, Phys. Rev. B **13**, 5188 (1976).
[26] A. Van der Ven, J. C. Thomas, Q. Xu, B. Swoboda, and D. Morgan, Phys. Rev. B **78**, 104306 (2008).
[27] B. Puchala and A. Van der Ven, Phys. Rev. B **88**, 094108 (2013).
[28] A. Togo, F. Oba, and I. Tanaka, Phys. Rev. B **78**, 134106 (2008).
[29] S. Baroni, A. Corso, S. Gironcoli, and P. Giannozzi, Rev. Mod. Phys. **73**, 515 (2001).
[30] X. Gonze and C. Lee, Phys. Rev. B **55**, 10355 (1997).
[31] K. Momma and F. Izumi, J. Appl. Crystallogr. **44**, 1272 (2011).
[32] P. Villars and L. D. Calvert, *Pearson's Handbook of Crystallographic Data for Intermetallic Phases* (American Society of Metals, Metals Park, OH, 1985).
[33] K. Kirievsky, Y. Gelbstein, and D. Fuks, J. Solid State Chem. **203**, 247 (2013).
[34] D. Jung, K. Kurosaki, C. Kim, H. Muta, and S. Yamanaka, J.Alloys Compd. **489**, 328 (2010).
[35] JW Cahn, Acta Metall. **10**, 179 (1962).
[36] A. Van der Ven, K. Garikipati, S. Kim, and M. Wagemaker, J. Electrochem. Soc. **156**, A949 (2009).
[37] S. V. Barabash, V. Ozoliņš, and C. Wolverton, Phys. Rev. B **78**, 214109 (2008).
[38] H. Chi, H. Kim, J. C. Thomas, X. Su, S. Stackhouse, M. Kaviany, A. Vander Ven, X. Tang, and C. Uher, Phys. Rev. B **86**, 195209 (2012).
[39] P. W. Voorhees, J. Stat. Phys. **38**, 231 (1985).
[40] L. Lindsay, D. A. Broido, and T. L. Reinecke, Phys. Rev. Lett. **111**, 025901 (2013).
[41] H. Özişik, K. Çolakoğlu, and H. B. Özişik, Fizika **16**, 154 (2010).
[42] D. Wee, B. Kozinsky, B. Pavan, and M. Fornari, J. Electron. Mater. **41**, 977 (2012).
[43] P. Hermet, K. Niedziolka and P. Jund, R. Soc. Chem. Adv. **3**, 22176 (2013)
[44] R. Kuentzler, R. Clad, G. Schmerber, and Y. Dossmann, J. Magn. Magn. Mater. **104**, 1976 (1992).
[45] B. Zhong, MS thesis, Iowa State University, 1997 (unpublished).
[46] W. Zhong, D. Vanderbilt, and K. M. Rabe, Phys. Rev. B **52**, 6301 (1995).
[47] J. Bhattacharya and A. Van der Ven, Acta Mater. **56**, 4226 (2008).
[48] J. C. Thomas and A. Van der Ven, Phys. Rev. B **88**, 214111 (2013).

[49] G. Grimvall, B. Magyari-Köpe, V. Ozoliņš, and K. A. Persson, Rev. Mod. Phys. **84**, 945 (2012).

[50] M. Fuchs, M. Bockstedte, E. Pehlke, and M. Scheffler, Phys. Rev. B **57**, 2134 (1998).

[51] H. A. Jahn and E. Teller, Proc. R. Soc. London, Ser. A **161**, 220 (1937).

[52] P. M. Galanakis and P. H. Dederichs, J. Phys. D: Appl. Phys. **39**, 765 (2006).